Comparative study of plasma excitations in single-walled carbon nanotubes and graphite by inelastic x-ray and electron scattering

C. Kramberger,[1] E. Einarsson,[2] S. Huotari,[3] T. Thurakitseree,[2] S. Maruyama,[2] M. Knupfer,[4] and T. Pichler[1]

[1]*University of Vienna, Faculty of Physics, Strudlhofgasse 4, A-1090, Vienna, Austria*

[2]*The University of Tokyo, Department of Mechanical Engineering, 7-3-1 Hongo, Bunkyo-ku, Tokyo 113-8656, Japan*

[3]*European Synchrotron Radiation Facility, Boîte Postale 220, F-38043 Grenoble Cedex 9, France*

[4]*IFW Dresden, Helmholtzstraße 20, D-01069 Dresden, Germany*

(Dated: submitted to Phys. Rev. B, January 25, 2010)

Abstract

The dynamical structure factor $S(q,\omega)$ in both graphite and freestanding thin-bundled single-walled carbon nanotubes (SWNTs) is probed by means of inelastic x-ray and electron scattering. We utilize the equivalency and complementarity of the two techniques in our combined approach. The plasmon dispersions provide direct insight into the imprints of macroscopic screening and low-dimensional confinement on excitonic inter-band transitions in SWNTs.

PACS numbers: 73.22.Lp

I. INTRODUCTION

The atoms in a flat, sp^2-bonded carbon sheet are arranged in a hexagonal honeycomb structure. The graphene sheet is the basic building block of hierarchical materials such as graphite or single-walled carbon nanotubes (SWNTs), which are essentially rolled-up strips of graphene. Different densities and dimensionalities may be constructed from the versatile carbon sheets. The local dimensionality as well as the macroscopic density are crucial for collective phenomena, such as charge-density waves[1–3] or effective exciton binding energies[4,5]. Charge-density waves can propagate in a solid, and posses a momentum state[6,7]. They may be accessed experimentally by inelastic scattering events, and stem from the loss-function that is readily derived from the complex dielectric function $\varepsilon(\omega)$ as $\phi(\omega) = \mathrm{Im}(-1/(\varepsilon(q,\omega)))$. The integral in the f-sum rule $\frac{\pi}{2}\omega_p^2 = \int d\omega\, \omega\phi(\omega)$, where the plasma frequency is introduced as $\omega_p^2 = n_e e^2/m_e\varepsilon_0$, scales with the density of electrons n_e. Thus, plasmon frequencies are upshifted at higher electron densities. Due to this screening, a plasmon's energy always lies above the corresponding inter-band transition.

A material's loss-function is composed of individual plasmons, that in conventional matter arise at the zeros of the real part of the generalized dielectric function $\mathrm{Re}(\varepsilon(q,\omega)) = 0$. In very thin media or in individual molecules, as well as, isolated nano-objects, there is however no sufficient collective charge carrier density to corroborate a vanishing $\mathrm{Re}(\varepsilon(q,\omega))$. In this cases the observed plasmons can no longer be envisaged as density waves in a plasma but they are constituted of material-specific electronic inter-band transitions.

To date, there have been two entirely independent approaches to experimentally probe the momentum-dependent loss function $\phi(q,\omega)$. These two approaches use either inelastically scattered x-rays or electrons, both of which may excite propagating plasmons for energies of several eV and momentum transfers of a few $\mathring{A}^{-1}$. Both methods probe the loss-function in their own unique way. From an experimental point of view the most crucial distinction lies in the magnitude as well as the different scaling of the cross-section with the scattering angle or momentum transfer q. The scalings are $\propto q^2$ for Thomson scattering and $\propto 1/q^2$ for Rutherford scattering of x-rays and electrons, respectively.

Here, we utilize archetypical sp^2 carbon systems like graphite and SWNTs to experimentally address the quantitative comparison of the momentum resolved loss-function as probed in inelastic x-ray scattering (IXS) and angle-resolved electron energy-loss spectroscopy (AR-

EELS). In addition to earlier studies[8,9] we probe the full angle resolved dispersion relation using both methods. Regarding the plasmon dispersion, thin-bundled SWNTs[10] reveal in comparison to bulk material a fundamental change in the shapes as well as a shift in the absolute positions. The very different plasmon dispersions at small to intermediate momentum transfers q are strongly contrasted by a uniform plasmon response in the limit of high q. These stark effects can be understood in terms of a wavelength dependent effective charge carrier density. They are ultimately imprints of the varied macroscopic charge carrier densities as well as the internal morphologies in the different superstructures of carbon sheets. Nano-structured sp^2 carbon architectures are a showcase example of a precisely tunable plasmon response and hence offer a significant potential for engineering purposes.

II. EXPERIMENTAL

Forests of vertically aligned and $\sim$ 50 μm long SWNTs were grown by chemical vapor deposition using alcohol vapor and a binary Co/Mo catalyst[11]. Two as-grown films were removed from their quartz substrates using warm water and transferred onto standard Cu TEM grids[12]. The total thickness of the stacked vertically aligned SWNTs is $\sim$ 100 μm. The grid-supported SWNTs as well as empty TEM reference grids were mounted over a 2 mm wide slit in a 20x20x1 mm steel plate. A 500 μm thick sample of turbostratic graphite was used as a reference for archetypical bulk sp^2 carbon.

IXS experiments were conducted at beamline ID16 of the E.S.R.F. in Grenoble[13]. The radiation from three consecutive undulators was monochromatized by a cryogenically cooled Si(111) premonochromator and a Si(220) channel-cut secondary monochromator. Si(660) analyzer crystals were used in the Rowland-circle geometry (bending radius 1 m). The total energy resolution in the measurements was 0.75 eV. Depending on the orientation of the samples, spectra were either recorded in transmission or reflection geometry. In the former the momentum transfer is perpendicular to and in the latter q is parallel to the net alignment of the SWNTs in the stacked films. The momentum transfer spread along the analyzer crystals was limited by slitting the analyzers down to $\Delta q = 0.1$ $\mathring{A}^{-1}$. The samples were measured at ambient temperature and under vacuum to avoid spurious x-ray scattering from air. Angle resolved electron energy-loss spectroscopy (AR-EELS) on a single crystal of graphite has been conducted previously[14], and this data is used here for the experimental

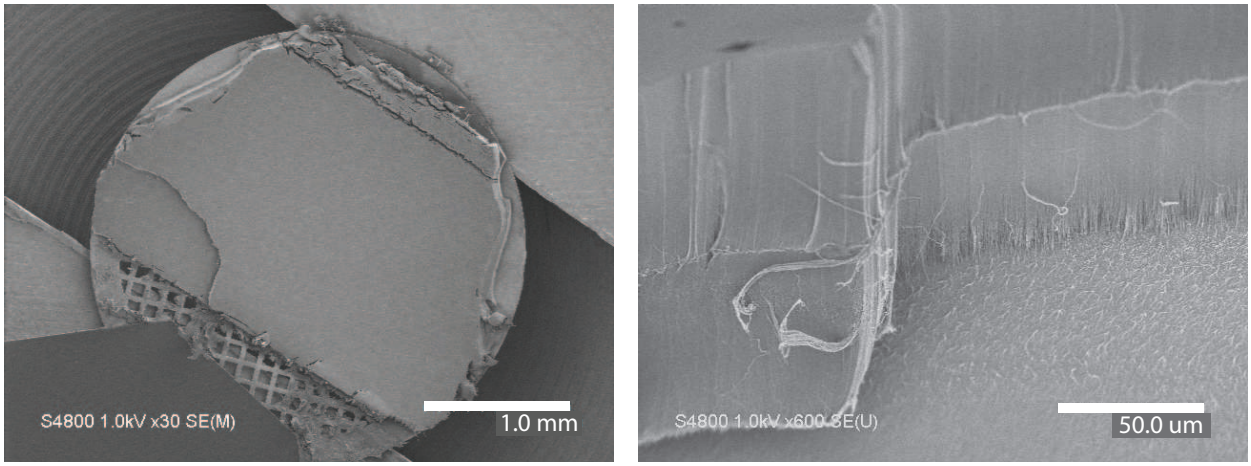

FIG. 1: *Left panel:* Overview SEM micrograph of the homogeneous double-layered sample on a TEM grid crossing the 2 mm wide gap in the sample holder. The only single-layered region can be seen on the left. *Right panel:* Perspective view of the bi-layer structure of thin-bundled SWNT forests. The micrographs were taken after the IXS measurements

comparison of IXS and AR-EELS.

The morphology of the vertically aligned SWNT double layer was confirmed before and after IXS measurements by scanning electron microscopy (SEM, Hitachi S-4800 operated at 1 kV).

III. RESULTS & DISCUSSION

In Fig. 1 we show the overall morphology of our thin-bundled SWNT forests. The micrographs taken after the IXS experiments clearly show that the majority of the sample area is indeed a uniform bi-layer structure, and that the height of each forest is ~ 50 μm.

The dispersive loss-functions of highly ordered pyrolytic graphite (HOPG) and thin-bundled SWNTs are shown in Fig. 2. The momentum transfer along the basal planes of the turbostratic layers in HOPG is reminiscent of the inherent spread of chiralities for q along the axis of the aligned SWNTs. The probed momentum transfers q extend from 0.5 up to 2.75 $\mathring{A}^{-1}$. The archetypical loss-function of all sp^2 carbon comprises the mono-modal π and the structured $\pi + \sigma$ plasmons. In the present case the dispersive π plasmon is observed between energy losses of 7 and 12 eV, and the maximum of the $\pi + \sigma$ plasmon is observed in the range between 20 and 40 eV. The in-plane average of HOPG is in excellent agreement

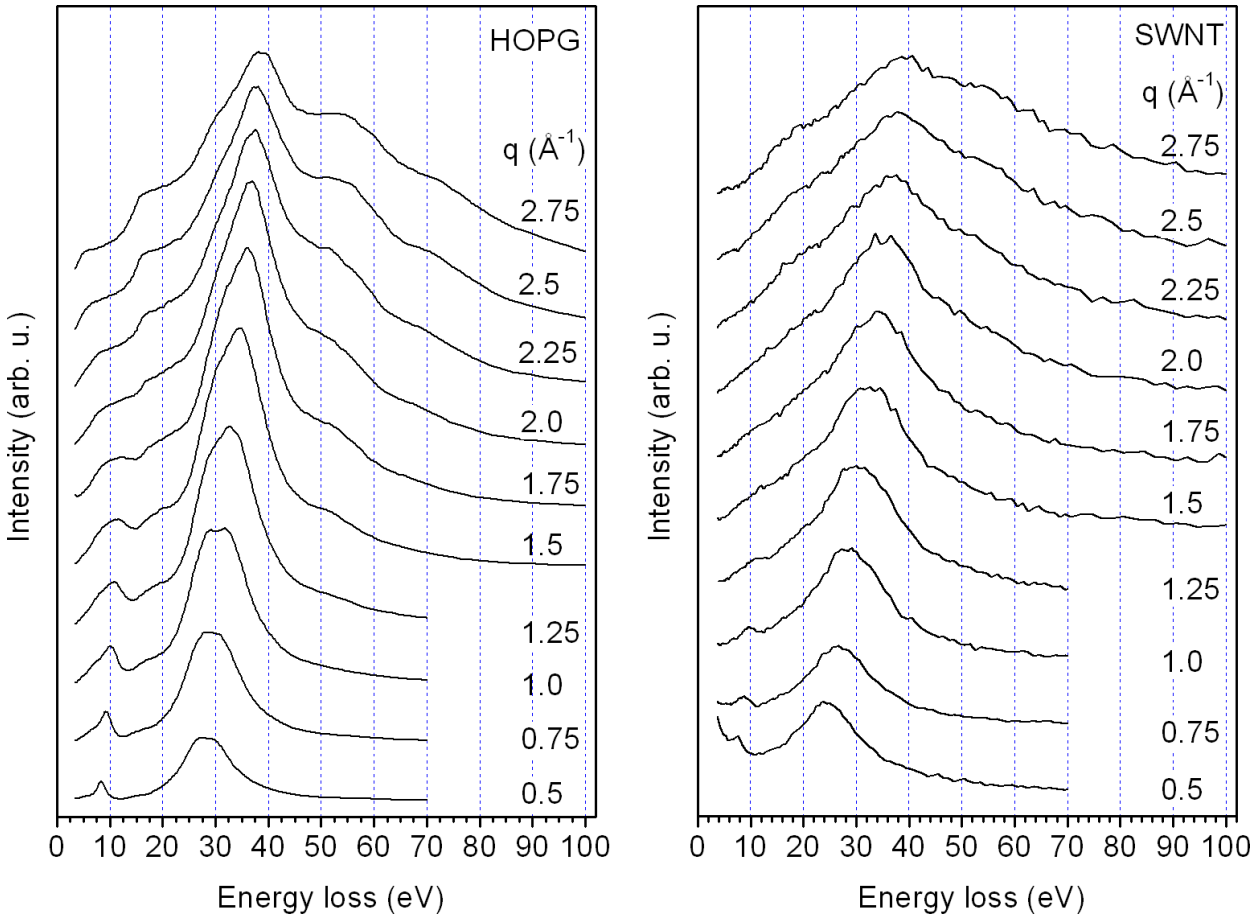

FIG. 2: (color online) *Left panel:* Loss-functions of HOPG as recorded at 9.68 keV for increasing q in the basal plane. *Right panel:* The corresponding loss-functions of a VA-SWNT film with q along the net alignment

with earlier IXS studies on a graphitic single crystal[15]. While most of the spectral features show a dispersive behavior, there is also one localized peak resolved at ∼15.5 eV. In earlier studies this feature, which becomes more pronounced at higher q, has been assigned to the non-dispersing c-axis $\sigma \rightarrow \sigma^{\star}$ response of graphite. The non-dispersing $\sigma \rightarrow \sigma^{\star}$ excitation may also be discerned in the aligned SWNTs at the same position. The σ electrons do not have a significant overlap with neighboring graphene sheets at the van der Waals distance of 3.4 $\mathring{A}$, thus the out-of-plane $\sigma \rightarrow \sigma^{\star}$ excitation is effectively localized to the plane and it is hence the same in either superstructure of sp^2 carbon sheets.

The overlap between neighboring sheets is only provided by the π electrons, either in the specific π or the collective $\pi + \sigma$ plasmon. These are in turn strongly affected by different densities in the graphite or thin bundled SWNT architecture. The energies of the dispersive

π and $\pi + \sigma$ plasmons in thin-bundled SWNTs are, as shown in Fig. 2, noticeably lowered with respect to bulk HOPG. Noteworthy, the shift in peak positions is only well observed at small q, but not found at high q.

In bulk graphite, the same upshift of in-plane plasmon frequencies[16] with respect to the inter-band transitions from optical absorption[17] is a long established finding. However in the present case we experimentally demonstrate that the effect of the macroscopic screening is strongly dependant on the actual character of a loss-feature. Plasmons that occur at real zeros of $\varepsilon(q, \omega)$ are strongly affected, but electronic excitations with a low oscillator strength show no noticeable shift with the charge carrier density. The direct comparison of the plasmon energies observed in the current IXS experiments with earlier AR-EELS results[2,18] on similar films of vertically aligned SWNTs reveals that the $\sim$100 μm-thick SWNTs films used currently have a noticeably higher macroscopic density than the thinner films that were used previously. The higher density of the present thin-bundled SWNT forests is an experimental necessity to perform inelastic x-ray scattering.

The dispersion of the $\pi + \sigma$ plasmon in graphite, measured by AR-EELS and IXS, is compared to the dispersion of the $\pi + \sigma$ plasmon in thin-bundled SWNTs in Fig. 3. The most striking observation is that the $\pi + \sigma$ dispersions along k_x (the armchair direction) in single-crystalline graphite[14] and the uniaxial in-plane $\pi + \sigma$ dispersion in HOPG lie on the same curve. The quantitative match of the dispersions of the $\pi + \sigma$ plasmon as measured in IXS and AR-EELS demonstrates explicitly that both methods are indeed accessing the very same specific plasmon excitations, and may be combined seamlessly. However, as the scattering angle and hence the momentum transfer q is varied, there is a crucial difference in the respective electron-electron or x-ray-electron scattering cross-sections involved. In AR-EELS the cross section scales as $1/q^2$, which renders it the method of choice for small q. In IXS, the cross-section increases with q^2, making it advantageous for measuring at higher momentum transfers. The combination of these equivalent techniques with complementary domains unlocks a wide range of q for the observation of the full dispersion relation of the electronic excitations.

The overall observation on the $\pi + \sigma$ plasmon dispersion in thin bundled SWNT, bundled SWNT and graphite is, that their plasmon energies differ greatly at small q on the left hand side in Fig. 3, but they have converged at high q on the right hand side. First the $\pi + \sigma$ plasmon dispersions of the two different batches of the present thin bundled and the earlier

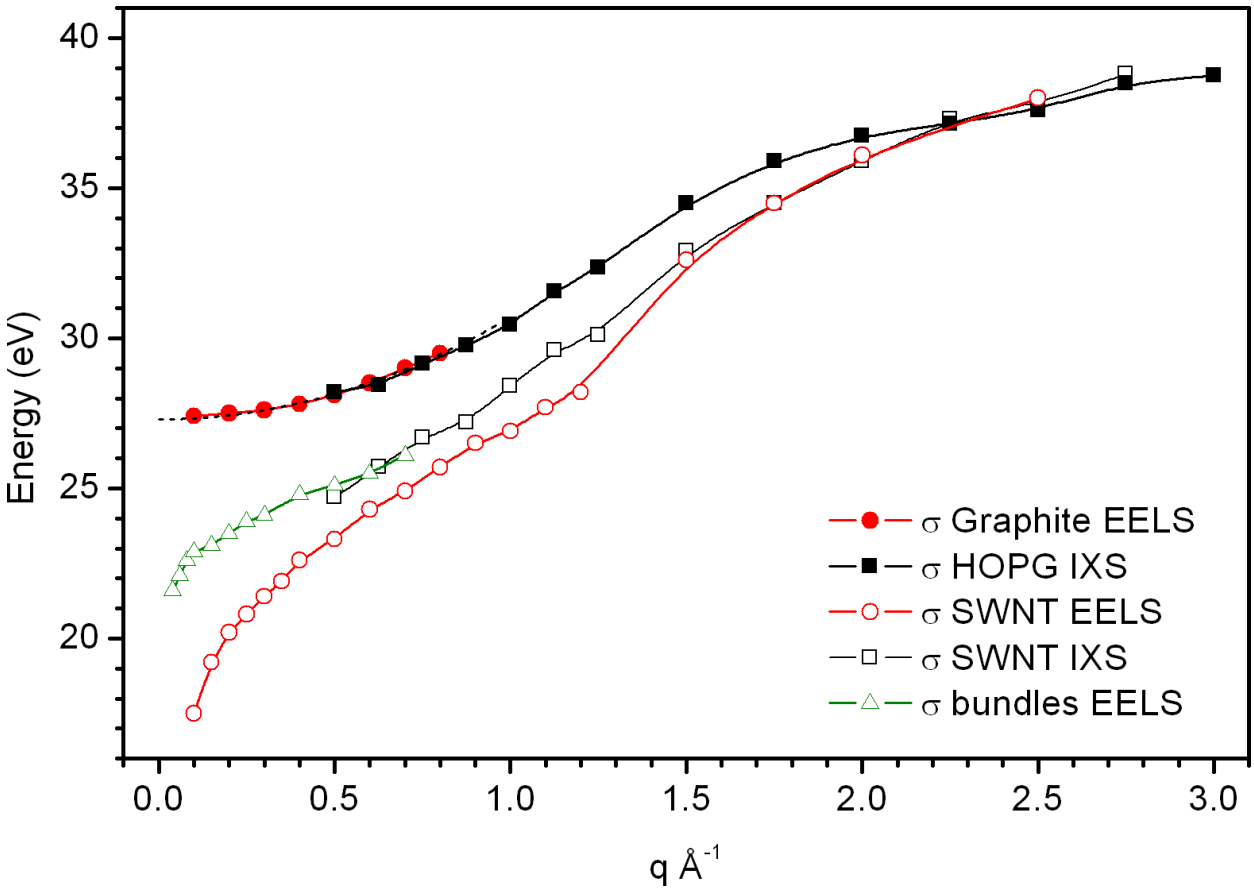

FIG. 3: (color online) Dispersion of the $\pi + \sigma$ plasmon in Graphite , bundled bulk SWNT and the VA-SWNT films

individual SWNTs converge, before only at the highest q even those of SWNT and HOPG meet. The slightly offset positions still agree well within the broadened peak widths. The non-uniform effect of the systems densities directly uncovers the evolution of the character of the loss-function with increasing q from collective plasmons to bare electronic inter-band excitations. Despite the very different model descriptions we observe a smooth transition from one to the other as the dielectric function evolves continuously[15].

Recent *ab-inito* calculations on $\phi(q, \omega)$ of single and bi-layer graphene[2], in the framework of time-dependent density functional theory with the inclusion of local field effects, provide quantitative insight into this interpretation. The long-reaching Coulomb interaction diminishes with decreasing wavelengths $\lambda = 1/q$ as λ^2. At small q and long λ, plasmons respond to the macroscopic screening from a large volume, but as q increases only the local density in a decreasing volume is probed. The momentum transfer q drives the transition from

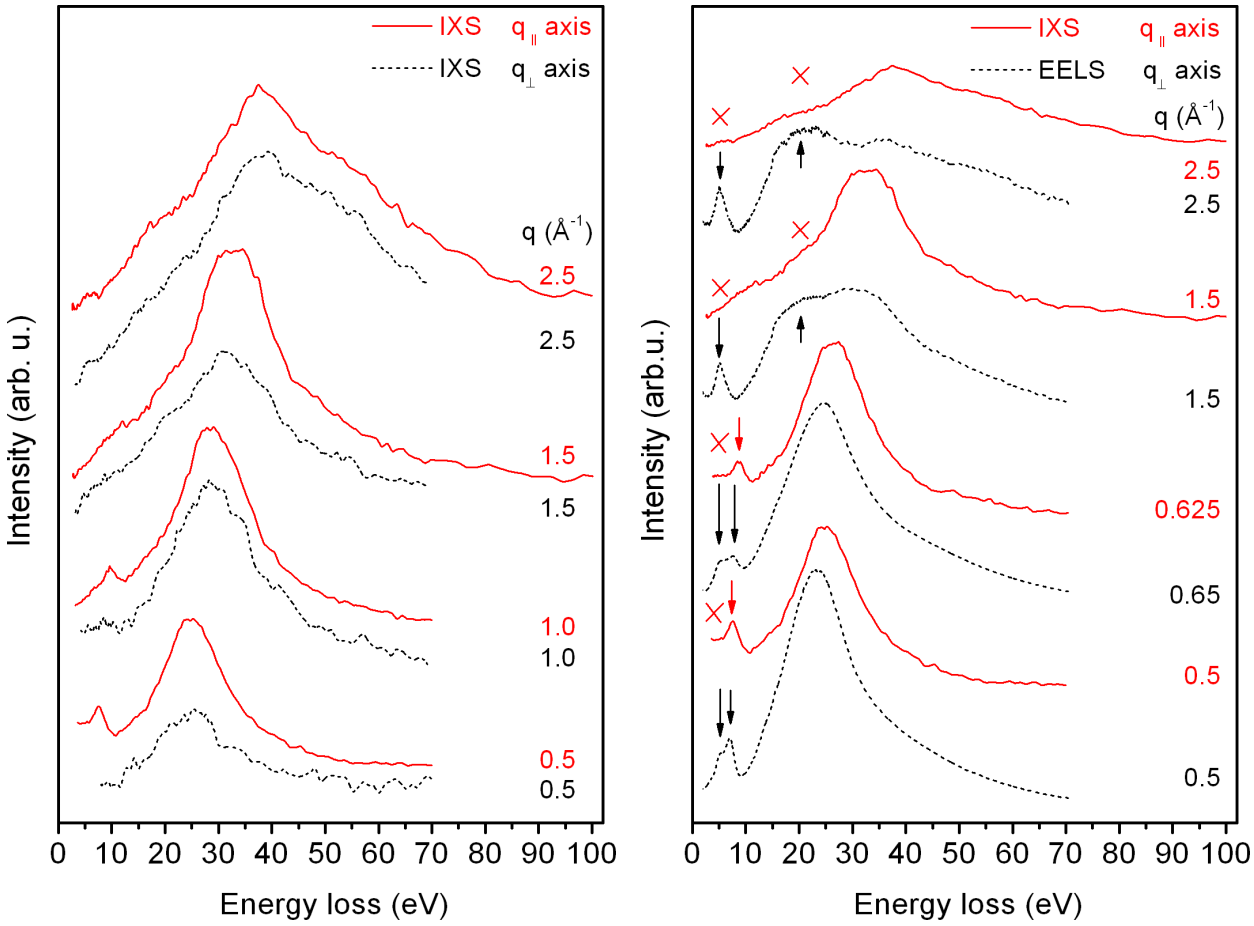

FIG. 4: (color online) *left panel:* Loss-functions of a VA-SWNT film as measured with IXS in transmission ($q_\perp$) and reflection ($q_\parallel$) geometry. *right panel:* The loss-function of VA-SWNT films as measured in transmissive ($q_\perp$) AR-EELS and reflective ($q_\parallel$) IXS

an unfocused probe of the density in the superstructure to a focused probe of the internal density. With the focused probe, there is no longer a distinction between sparse forests of thin-bundled SWNTs and bulk HOPG.

The loss-functions of thin bundled SWNTs as measured in transmission and reflection geometry are shown in Fig. 4 next to the comparison of the two SWNT batches loss-functions as measured in IXS and AR-EELS. In IXS we find that $q_\perp$ gives only a faint loss-function as compared to $q_\parallel$. This is a direct consequence of the alignment of the SWNTs perpendicular to the surface of the film. Plasmons with a certain q can in thin bundled SWNT only propagate along the bundles, so only the fraction of SWNT with suitable orientations for a given q vector can contribute to $\phi(q,\omega)$. The challenging low count rate and inferior statistics

for $q_\perp$ stem from the very diminutive fraction of tubes that are actually parallel to the films surface. Within the given statistics there is no substantial difference between $q_\perp$ and $q_\parallel$ for the same absolute value of q, other than the number of scattering tubes. AR-EELS is for technical reasons only possible in transmission geometry and is best suited for $q_\perp$. The same isotropy disregarding relative countrates for different scattering geometries around $q_\perp$ is observed in AR-EELS[18]. If a given SWNT, due to its actual orientation, contributes to $q_\perp$ scattering events then it does it in the very same way as those SWNTs that show up in $q_\parallel$.

The direct comparison of the loss-functions of thin bundled SWNT as measured in IXS and AR-EELS in Fig. 4 reveals a clear difference. While AR-EELS observes for the π as well as the $\pi + \sigma$ excitations always a pair of a dispersive and a localized loss-feature. There are always only the dispersive loss-features visible in IXS in either scattering geometry. While the two experiments are evidently a perfect match for propagating plasmons, there is a striking contrast for localized excitations. The internal morphology may not only continually alter plasmons, but it may also give rise to novel excitations. A SWNT or thin bundle of the latter is, in one direction, a wire, that supports propagating excitations with a defined momentum state. In the perpendicular plane it is an isolated quantum dot, where there may be localized excitations with discrete angular momenta. While interband transitions will definitely require more elaborate theoretical methods[7] it can be calculated directly[19] that all free charge carrier multipole excitations on a metallic rod are degenerate. The results in Fig. 4 are also unexpected within an alternative interpretation[20], that associates the π plasmon structure in AR-EELS with the distribution of chiralities in SWNT. Alternatively, the difference in the emergence of localized plasmons in the right panel of Fig. 4 may have two plausible causes. Firstly, the differences might originate from different local nanotube density distributions in the two batches of material. Secondly, although Fig. 3 demonstrates the equivalency of IXS and EELS in bulk materials, there might arise fundamental differences in the selection rules for electron and x-ray scattering in the realm of isolated nano-structures, where the dielectric response is governed by local field effects. In the latter context it is an entirely open issue if IXS experiments analogous to microscopic and angle integrated EELS experiments on nanotubes[8,9] could, in principle, retrieve the very same spatial distribution of plasmon modes.

The dispersion relations of the π plasmon in a graphite single crystal, turbostratic

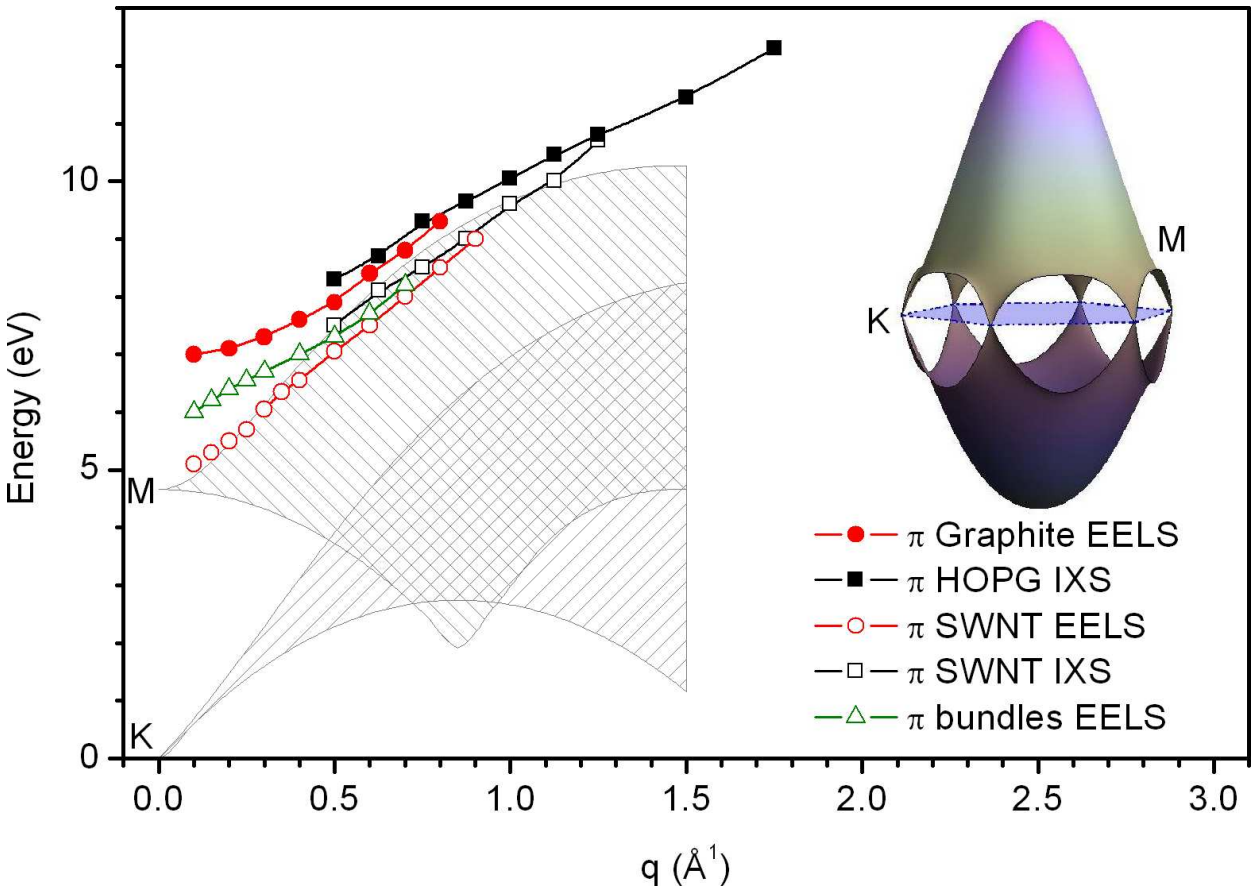

FIG. 5: (color online) Dispersion of the π plasmon in Graphite, bulk bundled SWNT and the VA-SWNT films. The shaded areas mark the domain of bare single-electron excitations rooting from either the K or the M point in the band structure of graphene, as shown in the inset

graphite, and thin-bundled SWNTs are displayed in Fig. 5. The π plasmon can be traced beyond 1 $\mathring{A}^{-1}$in HOPG and SWNTs before it can no longer be discerned from the onset of the structured $\pi+\sigma$ response. The anisotropy of the π plasmon in the plane of the graphene sheets is displayed in the mismatch of the in-plane averaged dispersion in HOPG and the dispersion along k_x (armchair direction) in the graphite single-crystal. Note, that the $\pi+\sigma$ dispersions in Fig. 3 are the same experimental data as in Fig. 2. The π plasmon is just like the $\pi+\sigma$ plasmon also evolving due to the changes in the effective electronic densities with increasing q. First, the π dispersions of the two batches of SWNTs with different densities meet before they branch into the dispersion of the HOPG. Since the optical limit at $q=0$ of the π dispersion in the thinner batch of SWNTs quantitatively matches optical absorbtion measurements[2,21] it is right from the beginning characterized as an inter-band transition.

The two-dimensional band structure of graphene is plotted in the inset of Fig. 5. We used a parameterized tight binding scheme that was fitted to *ab initio* GW calculations as well as angle-resolved photoemission experiments[22] on graphite. The shaded areas plotted together with the experimentally observed π plasmon dispersions show the range of energies accessible from the K point at the Fermi level as well as from the dominant van Hove singularity at the M point. Neither of these regions can directly corroborate the observed dispersion relation alone, which points at local field effects beyond the independent electron picture. The relevance of local field effects in isolated or bi-layer graphene was exemplified by clear deviations from the framework of independent particle transitions in the quantitative description of the linear π plasmon dispersion[2] as well as the optical absorption[23]. The present non-linear dispersion relations are proposed to be the result of a finite wavelength dependency of the local field effects in the different superstructures of sp^2 carbon. While such generalized local field effects offer a footing for a quantitative description of the observed dispersion relations, the mere complexity of these superstructures are to date beyond the reach of *ab initio* calculations.

IV. SUMMARY

We employ superstructures of sp^2 carbon sheets with different densities and effective dimensionalities to experimentally address the influence of the latter on the dynamics of archetypical π and $\pi + \sigma$ plasmons. The seamless joining of the $\pi + \sigma$ plasmon dispersions from IXS and AR-EELS demonstrates that electrons and x-rays are equivalent probes of inelastic scattering events, but they are accessing complementary domains in q. We observe that the itinerant π as well as the $\pi + \sigma$ plasmons are affected by the macroscopic density, while the localized $\sigma \rightarrow \sigma^\star$ plasmon is not. At low q, the energy of itinerant plasmons scales with the respective density before they turn only at high q into inter-band transitions. The cross-over from plasmons to excitonic inter-band transitions is concomitant to the weakening of the Coulomb interaction with $1/q^2$, which tunes the plasmon response from a macroscopic probe of the density in the superstructure to a local probe of the internal density. We propose this interpretation can be quantified in terms of wave length dependent local field effects in the dielectric response of carbon nano-structures. The quantitative knowledge on the realms of collective excitations and inter-band excitations in hierarchical materials is a crucial step

towards engineered electronic properties in man-made nano-structured materials.

Acknowledgements: EE acknowledges support from the Global Center of Excellence for Mechanical Systems Innovation" by the Japanese Ministry of Education, Culture, Sports, Science and Technology. TP acknowledges the DFG 440/3/5 and the FWF P21333-N20.

---

[1] S. DasSarma and E. H. Hwang, Phys. Rev. B **54**, 1936 (1996).

[2] C. Kramberger, R. Hambach, C. Giorgetti, M. H. Rummeli, M. Knupfer, J. Fink, B. Buchner, L. Reining, E. Einarsson, S. Maruyama, et al., Phys. Rev. Lett. **100**, 196803 (2008).

[3] M. F. Lin, Phys. Rev. B **62**, 13153 (2000).

[4] F. Wang, G. Dukovic, L. E. Brus, and T. F. Heinz, Science **308**, 838 (2005).

[5] C. D. Spataru, S. Ismail-Beigi, R. B. Capaz, and S. G. Louie, Quasiparticle and excitonic effects in the optical response of nanotubes and nanoribbons, vol. 111 of Topics in Applied Physics (Springer Verlag, Berlin Heidelberg, 2008).

[6] P. Nozieres and D. Pines, Phys. Rev. **113**, 1254 (1959).

[7] G. Onida, L. Reining, and A. Rubio, Rev. Mod. Phys. **74**, 601 (2002).

[8] M. H. Upton, R. F. Klie, J. P. Hill, T. Gog, D. Casa, W. Ku, Y. Zhu, M. Y. Sfeir, J. Misewich, G. Eres, et al., Carbon **47**, 162 (2009).

[9] M. Kociak, L. Henrard, O. Stephan, K. Suenaga, and C. Colliex, Phys. Rev. B **61**, 13936 (2000).

[10] E. Einarsson, H. Shiozawa, C. Kramberger, M. H. Rummeli, A. Gruneis, T. Pichler, and S. Maruyama, J. Phys. Chem. C **111**, 17861 (2007).

[11] S. Maruyama, E. Einarsson, Y. Murakami, and T. Edamura, Chem. Phys. Lett. **403**, 320 (2005).

[12] Y. Murakami and S. Maruyama, Chem. Phys. Lett. **422**, 575 (2006).

[13] R. Verbeni, T. Pylkkänen, S. Huotari, L. Simonelli, G. Vankó, K. Martel, C. Henriquet, and G. Monaco, Jour. of Sync. Rad. **16**, 469 (2009).

[14] A. G. Marinopoulos, L. Reining, V. Olevano, A. Rubio, T. Pichler, X. Liu, M. Knupfer, and J. Fink, Phys. Rev. Lett. **89**, 076402 (2002).

[15] N. Hiraoka, H. Ishii, I. Jarrige, and Y. Q. Cai, Phys. Rev. B **72**, 075103 (2005).

[16] K. Zeppenfeld, Zeitschrift f. Physik **211**, 391 (1968).

[17] E. A. Taft and H. R. Philipp, Phys. Rev. **138**, A197 (1965).

[18] C. Kramberger, M. Rummeli, M. Knupfer, J. Fink, B. Buchner, E. Einarsson, S. Maruyama,

and T. Pichler, Phys. Stat. Sol. B **245**, 2284 (2008).

[19] T. McNeish, G. Gumbs, and A. Balassis, Phys. Rev. B **77**, 235440 (2008).

[20] S. Dmitrovic, T. Vukovic, B. Nikolic, M. Damnjanovic, and I. Milosevic, Phys. Rev. B **77**, 245415 (2008).

[21] Y. Murakami, E. Einarsson, T. Edamura, and S. Maruyama, Phys. Rev. Lett. **94**, 087402 (2005).

[22] A. Gruneis, C. Attaccalite, L. Wirtz, H. Shiozawa, R. Saito, T. Pichler, and A. Rubio, Phys. Rev. B **78**, 205425 (2008).

[23] L. Yang, J. Deslippe, C. H. Park, M. L. Cohen, and S. G. Louie, Phys. Rev. Lett. **103**, 186802 (2009).